Data report: microstructure of chilled margins in the sheeted dike complex of IODP Hole 1256D[1]

Nicholas W. Hayman,[2] Ryo Anma,[3] and Eugenio E. Veloso[4]

Chapter contents

[1] Hayman, N.W., Anma, R., and Veloso, E.E, 2009. Data report: microstructure of chilled margins in the sheeted dike complex of IODP Hole 1256D. *In* Teagle, D.A.H., Alt, J.C., Umino, S., Miyashita, S., Banerjee, N.R., Wilson, D.S., and the Expedition 309/312 Scientists, *Proc. IODP,* 309/312: Washington, DC (Integrated Ocean Drilling Program Management International, Inc.). doi:10.2204/iodp.proc.309312.205.2009
[2] Institute for Geophysics, Jackson School for Geosciences, University of Texas, Austin TX 78758-4445, USA. **hayman@utig.ig.utexas.edu**
[3] Graduate School of Life and Environmental Sciences, University of Tsukuba, Ten-nodai 1-1-1, Tsukuba 305-8572, Japan.
[4] Facultad de Ingeniería y Ciencias Geológicas, Departamento Ciencias Geológicas, Universidad Católica del Norte, Avenue Angamos 0610, Antofagasta, Chile.

Abstract

Chilled margins were recovered from the sheeted dike complex (SDC) of superfast (>200 mm/y)-spreading East Pacific Rise–spread crust during drilling of Integrated Ocean Drilling Program Hole 1256D on the Cocos Plate. The chilled margins contain stretched spherules, oriented plagioclase laths, grain-size segregation, and color banding. These rheomorphs locally crosscut veins but are elsewhere crosscut by veins. Electron microprobe investigations found that the chilled margins comprise dispersed micrometer-scale minerals and veins including chlorite, actinolite, quartz, anhydrite, sphene, calcite, sphalerite, K-feldspar (adularia and/or orthoclase), magnetite, pyrite, and chalcopyrite. Though many of these phases are present throughout the SDC, anhydrite and calcite have not been previously recognized >100 m below the SDC–lava transition zone, and, with one exception, K-feldspar has not been previously identified in Hole 1256D core. Microstructures include quartz clasts surrounded by anhydrite, K-feldspar veins and clasts cut or surrounded by chilled margin material, and lenses of ductily deformed sphene. Some of the crosscutting relationships and distribution of mineral phases could be explained by hydrothermal alteration that occurred roughly simultaneously with dike intrusion.

Introduction

During Integrated Ocean Drilling Program (IODP) Expedition 312, the structural geology team was impressed by the microstructure of chilled margins recovered from the sheeted dike complex (SDC) of the Pacific crust drilled in Hole 1256D. Microstructures and crosscutting relationships within and around the chilled margins led the structure team to postulate that the fracturing and hydrothermal alteration of the chilled margins occurred more or less during dike intrusion. If so, the microstructures are evidence for weakening of the crust by elevated fluid pressure (Harper and Tartarroti, 1996; Umino et al., 2008) and provide a mechanism for the generation of hydrothermal plumes at the seafloor by diking (Delaney et al., 1998).

The purpose of this data report is to summarize shipboard observations of the SDC chilled margins and to present new, higher resolution data on the microstructures, mineralogy, and compositions of the dike margins. We review shipboard hand sample and thin section studies and present new backscatter electron images (BSEI)

doi:10.2204/iodp.proc.309312.205.2009

of chilled margins. We report on qualitative identification of phases from electron dispersive spectroscopy (EDS). Also presented are some wavelength dispersive spectroscopy (WDS) analyses of feldspars in the chilled margins; the feldspars preserve alteration microstructures, including K-feldspar zoning and variable barium concentrations. Other hydrothermal phases include lenses of anhydrite, sphene, and more widely reported hydrothermal minerals such as albite, chlorite, actinolite, calcite, and quartz. We close with a brief discussion of the probable origin and significance of the microstructure, mineralogy, and composition of the chilled margins.

Downhole distribution of chilled margins

The top of the SDC is defined by the conspicuous change with depth from sheet flows to massive basalts ~1060.9 meters below seafloor (mbsf) (see the **"Expedition 309/312 summary"** chapter) (Fig. **F1**). The base of the SDC is defined by the uppermost gabbroic intrusion at 1404.6 mbsf (Wilson et al., 2006). Recovery within the SDC was highly variable but averaged <12%. Above 1348 mbsf, 25 chilled margins and igneous contacts (dike boundaries without clear chilled margins) were recovered, 13 of these associated with densely fractured or veined (brecciated) basalt. The structure log tabulates the depths and orientations of these structures (see LOGS in **"Supplementary material"**).

The dikes are mostly steeply dipping, with 15 of the 25 oriented samples containing igneous contacts dipping 70°–90° in the core reference frame. However, several igneous contacts dip <70° and some dip <50° (Fig. **F1**) (see Fig. **F312** in the "Site 1256" chapter). A recent study of logging data by Tominaga et al. (2009) indicates that the dikes dip to the northeast.

Samples from core recovered from the SDC below ~1348 mbsf were pervasively recrystallized to a granoblastic texture inside the contact aureole of the underlying gabbro body (see the **"Expedition 309/312 summary"** chapter; Koepke et al., 2008). No chilled margins of dikes were recognized in this lowermost interval, presumably owing to a combination of low recovery and a strong metamorphic overprint.

Shipboard observations of chilled margins

During Expedition 312, the structure team compiled detailed observations of hand samples and thin sections (with polarized light microscopy). We summarize those observations here, with links to the relevant figures in the "Site 1256" chapter of this volume. Kempton (1985) compiled similar observations from Deep Sea Drilling Project/Ocean Drilling Program (DSDP/ODP) Hole 504B.

Chilled margins are the fine-grained intrusive contacts where aphanitic edges of (younger) dikes are in direct contact with the coarser-grained (older) dikes (see Fig. **F299** in the "Site 1256" chapter).

Variations in grain size, abundance of spherules, and alteration cause weak color banding parallel to the chilled margins. In aphanitic to finer grained parts of chilled margins, "rheomorphs"—indicators of flow age when the rock was in a molten state such as flow banding and stretched spherules—are inclined (~10° from parallelism) toward the chilled margin. Where grain size is coarse enough, plagioclase laths are generally oriented parallel to the chilled margins (see Fig. **F294** in the "Site 1256" chapter).

In other samples there are few flow indicators, and in one instance the spherulitic texture forms a wavy pattern along the dike margin, potentially indicating static cooling; that is, cooling after magma ceased flowing through the dike conduit (see Fig. **F299F, F299G** in the "Site 1256" chapter).

A feature near many chilled margins is thin (<1 cm) intrusions of glassy to aphanitic basalt. In some samples these intrusions are apophyses that enclose clasts derived from the adjacent coarser grained basalt (see Fig. **F300A–F300E** in the "Site 1256" chapter). Elsewhere, intrusions are aphanitic to glassy basalt in veinlets or en echelon cracks adjacent to the main chilled margin (see Figs. **F299H, F300B** in the "Site 1256" chapter).

Chilled margins in many samples are riddled with chlorite and actinolite veins. In some samples veins are crosscut and offset by laminations in the chilled margin, whereas other veins crosscut the chilled margins (see Fig. **F302** in the "Site 1256" chapter).

Where the crosscutting relations between veins and chilled margins are especially chaotic, the chilled margin was classified as a "dike-margin breccia" (see Fig. **F301** in the "Site 1256" chapter).

Backscatter electron images and electron dispersive spectroscopy of chilled margins

Structures shown previously within and around chilled margins are difficult to study in hand sample and optical microscopy alone; grains can be a few micrometers to submicrometer in size, and certain phases are intermixed and indistinguishable in transmitted light. To better document these important features, we present a collection of BSEI in Fig-

ures F2, F3, F4, F5, and F6. The images were taken from areas either within, adjacent to, or at the contact of chilled margins. The thin sections studied are indicated in Figure F1 at their approximate depth. For a detailed view of thin section images, refer to "Core descriptions."

All images were taken with the University of Texas Department of Geological Sciences JEOL-8200 electron microprobe in backscatter mode at a voltage of 15 kV and a current of 15 nA.

The host rock or wallrock immediately adjacent to the chilled margins is texturally similar to the interior of the dikes with subophitic textures defined by feldspar and pyroxene or amphibole. At shallower depths, relatively unaltered clinopyroxene partially surrounds a mixture of albite and anorthite, with interstitial calcite and small grains of sphalerite locally present (Fig. F2A); we note that calcium carbonate is otherwise relatively scarce in Hole 1256D below the lavas (Coggon et al., 2006). In deeper sections, clinopyroxene is completely replaced by actinolite (and/or actinolitic hornblende) and feldspars are a mixture of albite and anorthite (Fig. F2B).

The chilled margins define relatively sharp and clean contacts with the wallrocks, cutting phenocrysts of feldspar and pyroxene (Fig. F2C). At relatively shallow levels of the SDC, the chilled margins comprise an aphanitic mixture of clinopyroxene and albite (replacing plagioclase) (Fig. F2D). Locally and at deeper levels, micrometer-scale mixtures of clinopyroxene and feldspar define the texture of relatively unaltered chilled margins, possibly an original "quench" texture (Fig. F2E).

In hand sample and thin section, the defining quality of many chilled margins is color banding from dark gray to dark to medium green. There is no obvious change in grain size across these bands. In BSEI (with EDS), banding is due to variations in Fe content of aphantitic actinolite (Fig. F2F).

A variety of detailed microstructures are preferentially preserved in chilled margins that are indicative of magmatic flow, such as feldspar laths with preferred orientations (Fig. F3A). In Figure F3A, aphanitic (possibly submicrometer) material of chlorite composition surrounds the feldspar laths. Other flow and quench microstructures include widely disseminated micrometer-scale magnetite grains (Fig. F3B) likely formed during devitrification of glassy basalt; microfolds defined by aphanitic, finely mixed albite and chlorite (and adjacent vugs filled with actinolite) (Fig. F3C, F3D); spherules composed of actinolite and albite-anorthite (Fig. F3E); and clasts of feldspar suspended in the chilled margin (Fig. F3F).

One of the more extraordinary microstructures in hand sample, thin section, and BSEI are lenses of material oriented parallel to and stretched along the chilled margins. In a sample from Section 312-1256D-176R-2 a lens of titanite (sphene) is deformed along a chilled margin (Fig. F4A) (a similar example from Pacific crust exposed in the Hess Deep Rift is presented in Hayman and Karson, 2007). A chlorite-actinolite vein cuts the lens, though the composition changes along the trace of the vein. In other chilled margins veins are more homogeneous, in many places with actinolite (and/or chlorite) surrounded by albite (Fig. F4B). In Figure F4B, the composite actinolite-albite vein crosscuts stretched spherules and other rheomorphs but has relatively irregular vein walls. Elsewhere, actinolite fills vugs within albite veins, in turn crosscutting actinolite-rich areas of the chilled margin (Fig. F4C).

Some additional microstructures resulting from hydrothermal alteration include lenses of aphantic aggregates of chlorite that "wrap" around the chilled margin (Fig. F5A), nodules of quartz and chlorite within otherwise unaltered host rock (Fig. F5B), nodules of quartz suspended within chlorite-actinolite and anhydrite (Fig. F5C), and concentrated nodules of pyrite surrounded by quartz (Fig. F5D). Anhydrite is also found within the chilled margins, either along actinolite-chlorite veins (Fig. F5E) or as interstitial nodules surrounded by quartz and needles of iron oxides (Fig. F5F); initial thermomagnetic analyses confirm that magnetite is the main iron oxide phase in most dike-rock samples.

The last suite of BSEIs of note are shown in Figure F6, where feldspars adjacent to the chilled margins show a "mottled" alteration texture, in places enriched in potassium. Such orthoclase (or its low-temperature equivalent, adularia) enrichment appears to be localized to the host rock adjacent to the chilled margins or clasts suspended within the chilled margins (Fig. F6A–F6C, F6E, F6F). In places, orthoclase-rich grains are found adjacent to chlorite veins (Fig. F6D), but here, too, the orthoclase enrichment is spatially associated with the chilled margin.

Wavelength dispersive spectroscopy of feldspar grains

Intrigued by the orthoclase in feldspars along chilled margins, we collected WDS data from eight grains in two different thin sections. Analytical standards included anorthoclase, orthoclase, and albite. We analyzed for Na_2O, K_2O, CaO, SiO_2, and Al_2O_3 weight percent, along with SrO and BaO (Table T1). All analyses have a precision of <0.5%, with the exception of BaO (3.71%). We did not analyze for FeO and MgO,

which are presumably present in trace amounts. Probe conditions for quantitative analysis were the same as for imaging, with a beam diameter set at ~1 µm. Such a narrow beam diameter allowed analysis of spatially heterogeneous alteration patterns (as shown in Fig. F6), though it unfortunately led to several discarded analyses (owing to beam damage and/or enhanced cation diffusion); analyses with totals of 98–102 wt% were considered acceptable.

Plagioclase (anorthite-albite) compositions range from ~25% to 100% albite, whereas the alkalai feldspars (albite-orthoclase) compositions range from ~0% to 100% orthoclase (Fig. F7A). Two alkalai feldspars have unusually high CaO concentrations. There is no obvious dependency on feldspar composition and microstructural position (see Table T1, Structure column), depth, or grain habit.

Lastly, we compare SrO and BaO concentrations (Fig. F7B) and K_2O and BaO concentrations; there is a weak, positive correlation between K_2O and BaO. These were the only possible visual correlations after systematically plotting SrO and BaO against the other oxides.

Discussion and conclusions

The assemblage of anhydrite; quartz; and calcite, pyrite, sphalerite, and chalcopyrite is widely interpreted to result from hydrothermal alteration of basalts (e.g., Alt et al., 1996). Anhydrite potentially indicates the *rapid* mixing of hydrothermal fluids and seawater (e.g., Bethke, 1996). Quartz clasts suspended in anhydrite (Fig. F5C) is a structure that is reminiscent of discharge zones of hydrothermal vents (Delaney et al., 1987; Saccocia and Gillis, 1995). The enclosure of needlelike iron oxides in quartz (Fig. F5F) and vugs of quartz + chlorite in otherwise unaltered basalt (Fig. F5B) also reflect a disequilibrium system such as that found in high-temperature hydrothermal systems. Lastly, lenses of sphene require high-pH fluids to mobilize and concentrate titanium (Fig. F4A).

The local presence of potassium-rich alkalai feldspars (in some cases rich in SrO and/or BaO) is also indicative of hydrothermal alteration. A mineralized breccia from Core 309-1256D-122R also contained some alkalai feldspar (J.C. Alt, pers. comm., 2008), but otherwise, potassium-rich feldspars are not widely reported in Hole 1256D or in ocean crustal rocks in general. Microstructural relationships provide some information about the relative timing of the alteration that led to the K-feldspars. For example, the feldspar phenocryst in Figure F6A is crosscut by the chilled margin that has a dominantly chloritic composition and does not have elevated potassium concentrations. In another example, in Figure F6C, a potassium-rich feldspar clast is suspended in and appears to have reacted with the surrounding chilled margin. In other words, the potassium alteration must have occurred before (or during) the formation of the chilled margin. Although K-feldspars could signify aluminum mobility, such as that reported in lower temperature (~220°C) alteration of hyaloclastites (e.g., Zierenberg et al., 1995), they could equally reflect cation mobility, and such low temperatures did not likely prevail in the intrusive center where the chilled margin crosscutting relationships developed.

Many of the hydrothermal microstructures and minerals, such as the actinolite-chlorite-albite assemblage in veins and vugs (e.g., Fig. F5), are found in more generally hydrothermally altered basalt, away from dike margins, and likely grew over a range of time scales and temperatures. In contrast, the Expedition 312 structural geology team preferred the interpretation that *some* of the microstructural crosscutting relationships formed roughly simultaneous with dike emplacement, a process inferred in modern ridge settings (Delaney et al., 1998; Curewitz and Karson, 1998). Several of the chilled margin phases and microstructures are not found in other parts of Hole 1256D. Anhydrite, for example, is reported in cores recovered from the lavas and the upper portion of the SDC but is otherwise not thought to be widespread in the SDC (see the **"Expedition 309/312 summary"** chapter). The microstructure of the stretched lenses of sphene is unique to chilled margins and likely required relatively high temperature ductile deformation, such as that found along a cooling dike margin. In Hole 1256D, K-feldspars are only found in the host rock adjacent to or within the chilled margins, and the potassium alteration occurred prior to the more widespread alteration. Crosscutting relationships in scanning electron microscopy between altered clasts and grains of secondary minerals and the surrounding chilled margins certainly leaves open the hypothesis of synintrusion hydrothermal alteration. Further investigation of the Hole 1256D chilled margins using in situ isotopic analysis and more detailed and high-resolution mineralogy could potentially test this hypothesis further, and future drilling and submersible investigations of other ocean crustal localities could help determine the geologic record of intrusion-related hydrothermal fluid flow.

Acknowledgments

Samples and data were provided by the Integrated Ocean Drilling Program (IODP). Hayman was sup-

ported by the U.S. Science Support Program and National Science foundation OCE-0222154 (to J.A. Karson). Additional support provided by the John A. and Katherine G. Jackson School of Geosciences and the Geology Foundation at the University of Texas at Austin. Veloso and Anma acknowledge the support of Japan Marine Science and Technology Center and Institute for Frontier Research on Earth Evolution. We thank an anonymous reviewer for helpful suggestions.

References

Alt, J.C., Laverne, C., Vanko, D.A., Tartarotti, P., Teagle, D.A.H., Bach, W., Zuleger, E., Erzinger, J., Honnorez, J., Pezard, P.A., Becker, K., Salisbury, M.H., and Wilkens, R.H., 1996. Hydrothermal alteration of a section of upper oceanic crust in the eastern equatorial Pacific: a synthesis of results from Site 504 (DSDP Legs 69, 70, and 83, and ODP Legs 111, 137, 140, and 148.) *In* Alt, J.C., Kinoshita, H., Stokking, L.B., and Michael, P.J. (Eds.), *Proc. ODP, Sci. Results,* 148: College Station, TX (Ocean Drilling Program), 417–434. **doi:10.2973/odp.proc.sr.148.159.1996**

Bethke, C., 1996. *Geochemical Reaction Modeling: Concepts and Applications:* New York, NY (Oxford Univ. Press USA).

Coggon, R.M., Teagle, D.A.H., Cooper, M.J., Hayes, T.E.F., and Green, D.R.H, 2006. Data report: compositions of calcium carbonate veins from superfast spreading rate crust, ODP Leg 206. *In* Teagle, D.A.H., Wilson, D.S., Acton, G.D., and Vanko, D.A. (Eds.), *Proc. ODP, Sci. Results,* 206: College Station, TX (Ocean Drilling Program), 1–6. **doi:10.2973/odp.proc.sr.206.002.2006**

Curewitz, D., and Karson, J.A., 1998. Geological consequences of dike intrusion at mid-ocean ridge spreading centers. *In* Buck, W.R., Delaney, J.R., Karson, J.A., and Lagabrielle, Y. (Eds.), *Faulting and Magmatism at Mid-Ocean Ridges:* Washington, DC (Am. Geophys. Union), 117–136.

Delaney, J.R., Mogk, D.W., and Mottl, M.J., 1987. Quartz-cemented breccias from the Mid-Atlantic Ridge: samples of a high-salinity hydrothermal upflow zone. *J. Geophys. Res., [Solid Earth],* 92(B9):9175–9192. **doi:10.1029/JB092iB09p09175**

Delaney, J.R., Kelley, D.S., Lilley, M.D., Butterfield, D.A., Baross, J.A., Wilcock, W.S.D., Embley, R.W., and Summit, M., 1998. The quantum event of oceanic crustal accretion: impacts of diking at mid-ocean ridges. *Science,* 281(5374):222–230. **doi:10.1126/science.281.5374.222**

Harper, G.D., and Tartarotti, P., 1996. Structural evolution of upper Layer 2, Hole 896A. *In* Alt, J.C., Kinoshita, H., Stokking, L.B., and Michael, P.J. (Eds.), *Proc. ODP, Sci. Results,* 148: College Station, TX (Ocean Drilling Program), 245–259. **doi:10.2973/odp.proc.sr.148.132.1996**

Hayman, N.W., and Karson, J.A., 2007. Faults and damage zones in fast-spread crust exposed on the north wall of the Hess Deep Rift: conduits and seals in seafloor hydrothermal systems. *Geochem., Geophys., Geosyst.,* 8(10):Q10002. **doi:10.1029/2007GC001623**

Kempton, P.D., 1985. An interpretation of contrasting nucleation and growth histories from the petrographic analysis of pillow and dike chilled margins, Hole 504B, Deep Sea Drilling Project, Leg 83. *In* Anderson, R.N., Honnorez, J., Becker, K., et al., *Init. Repts. DSDP,* 83: Washington, DC (U.S. Govt. Printing Office), 165–181. **doi:10.2973/dsdp.proc.83.105.1985**

Koepke, J., Christie, D.M., Dziony, W., Holtz, F., Lattard, D., Maclennan, J., Park, S., Scheibner, B., Yamasaki, T., and Yamazaki, S., 2008. Petrography of the dike–gabbro transition at IDOP Site 1256 (equatorial Pacific): the evolution of the granoblastic dikes. *Geochem. Geophys. Geosyst.*, 9(7):Q07O09. **doi:10.1029/2008GC001939**

Saccocia, P.J., and Gillis, K.M., 1995. Hydrothermal upflow zones in the oceanic crust. *Earth Planet. Sci. Lett.,* 136(1–2):1–16. **doi:10.1016/0012-821X(95)00155-5**

Tominaga, M., Teagle, D.A.H., Alt, J.C., and Umino, S., 2009. Determination of volcanostratigraphy of the oceanic crust formed at superfast spreading ridge: electrofacies analyses of ODP/IOPD Hole 1256D. *Geochem., Geophys., Geosyst.,* 10(1):Q01003. **doi:10.1029/2008GC002143**

Umino, S., Crispini, L., Tartarotti, P., Teagle, D.A.H., Alt, J.C., Miyashita, S., and Banerjee, N.R., 2008. Origin of the sheeted dike complex at superfast spread East Pacific Rise revealed by deep ocean crust drilling at Ocean Drilling Program Hole 1256D. *Geochem., Geophys., Geosyst.,* 9(6):Q06O08. **doi:10.1029/2007GC001760**

Wilson, D.S., Teagle, D.A.H., Alt, J.C., Banerjee, N.R., Umino, S., Miyashita, S., Acton, G.D., Anma, R., Barr, S.R., Belghoul, A., Carlut, J., Christie, D.M., Coggon, R.M., Cooper, K.M., Cordier, C., Crispini, L., Durand, S.R., Einaudi, F., Galli, L., Gao, Y., Geldmacher, J., Gilbert, L.A., Hayman, N.W., Herrero-Bervera, E., Hirano, N., Holter, S., Ingle, S., Jiang, S., Kalberkamp, U. Kerneklian, M., Koepke, J., Laverne, C., Vasquez, H.L.L., Maclennan, J., Morgan, S., Neo, N., Nichols, H.J., Park, S.-H., Reichow, M.K., Sakuyama, T., Sano, T., Sandwell, R., Scheibner, B., Smith-Duque, C.E., Swift, S.A., Tartarotti, P., Tikku, A.A., Tominaga, M., Veloso, E.A., Yamasaki, T., Yamazaki, S., and Ziegler, C., 2006. Drilling to gabbro in intact ocean crust. *Science,* 312(5776):1016–1020. **doi:10.1126/science.1126090**

Zierenberg, R.A., Schiffman, P., Jonasson, I.R., Tosdal, R., Pickthorn, W., and McClain, J., 1995. Alteration of basalt hyaloclastite at the off-axis Sea Cliff hydrothermal field, Gorda Ridge. *Chem. Geol.,* 126(2):77–99. **doi:10.1016/0009-2541(95)00111-2**

Initial receipt: 8 December 2008
Acceptance: 22 May 2009
Publication: 9 July 2009
MS 309312-205

Figure F1. Downhole distribution of recovery. Recovery is in relative percent. Microprobe observations made at the University of Texas. * = wavelength dispersive spectroscopy analyses of feldspars. See text and the "Expedition 309/312 summary" chapter for more detail.

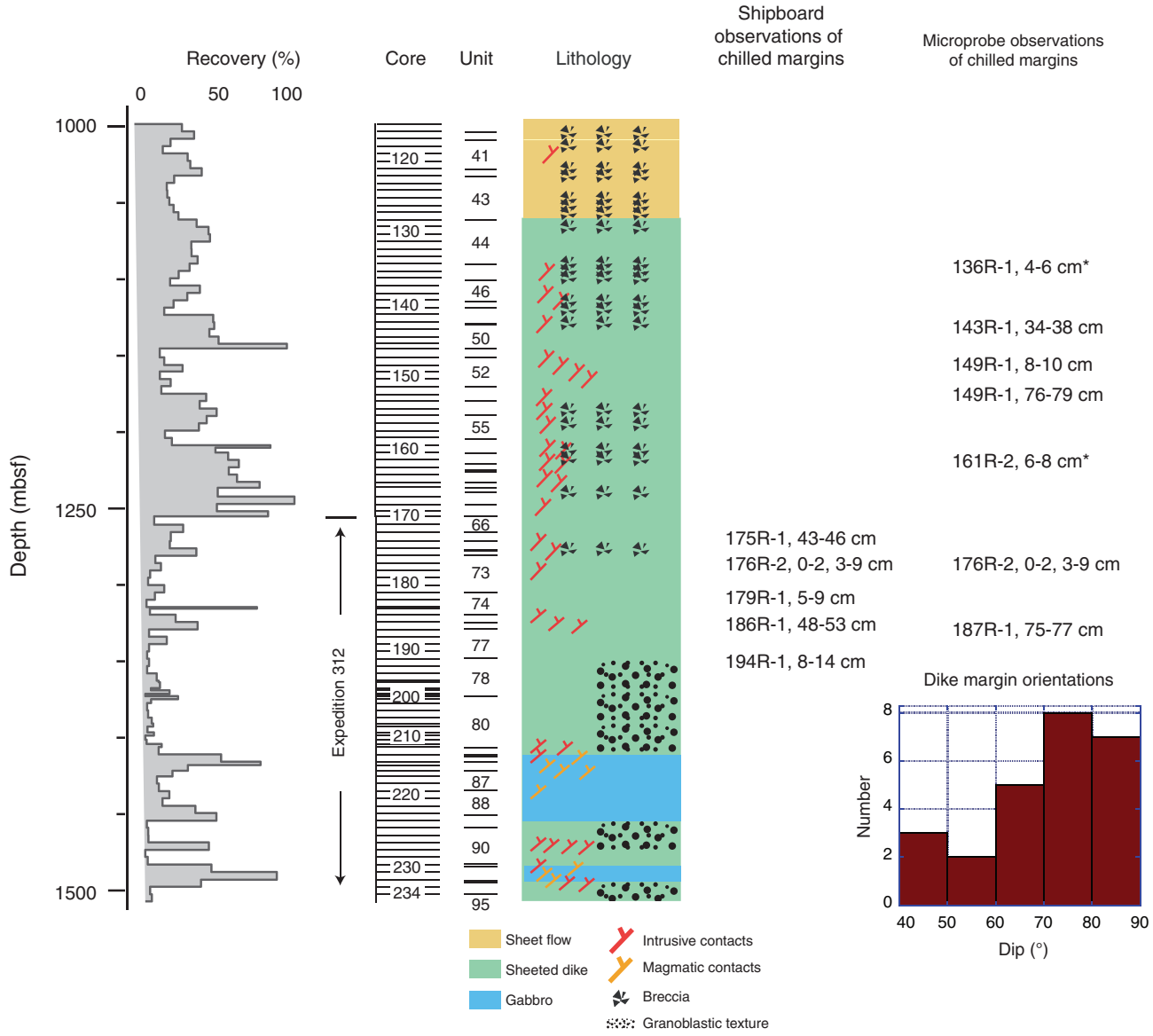

Figure F2. Backscattered electron imaging photomicrographs of microstructure of host rock and chilled margins. **A.** Fine- to medium-grained subophitic texture with clinopyroxene (CPX) and feldspar (anorthite is slightly lighter gray than albite [Ab]) (Sample 309-1256D-136R-1, 4–6 cm). Interstitial secondary minerals include sphalerite (ZnS) and calcite (Cte). **B.** Actinolite (Act) and mixed albite and anorthite (Ab-An) feldspars with interstitial FeO (Sample 312-1256D-187R-1, 75–77 cm). **C.** Chilled margin (top right) (Sample 309-1256D-136R-1, 4–6 cm). **D.** Finely mixed clinopyroxene and albite in a chilled margin (Sample 309-1256D-136R-1, 4–6 cm). **E.** Mixed clinopyroxene and mixed albite-anorthite within the chilled margin (Sample 309-1256D-161R-2, 6–8 cm). **F.** Banding in a chilled margin defined by variations in Fe concentration in actinolite, determined by electron dispersive spectroscopy (Sample 309-1256D-143R-1, 34–38 cm).

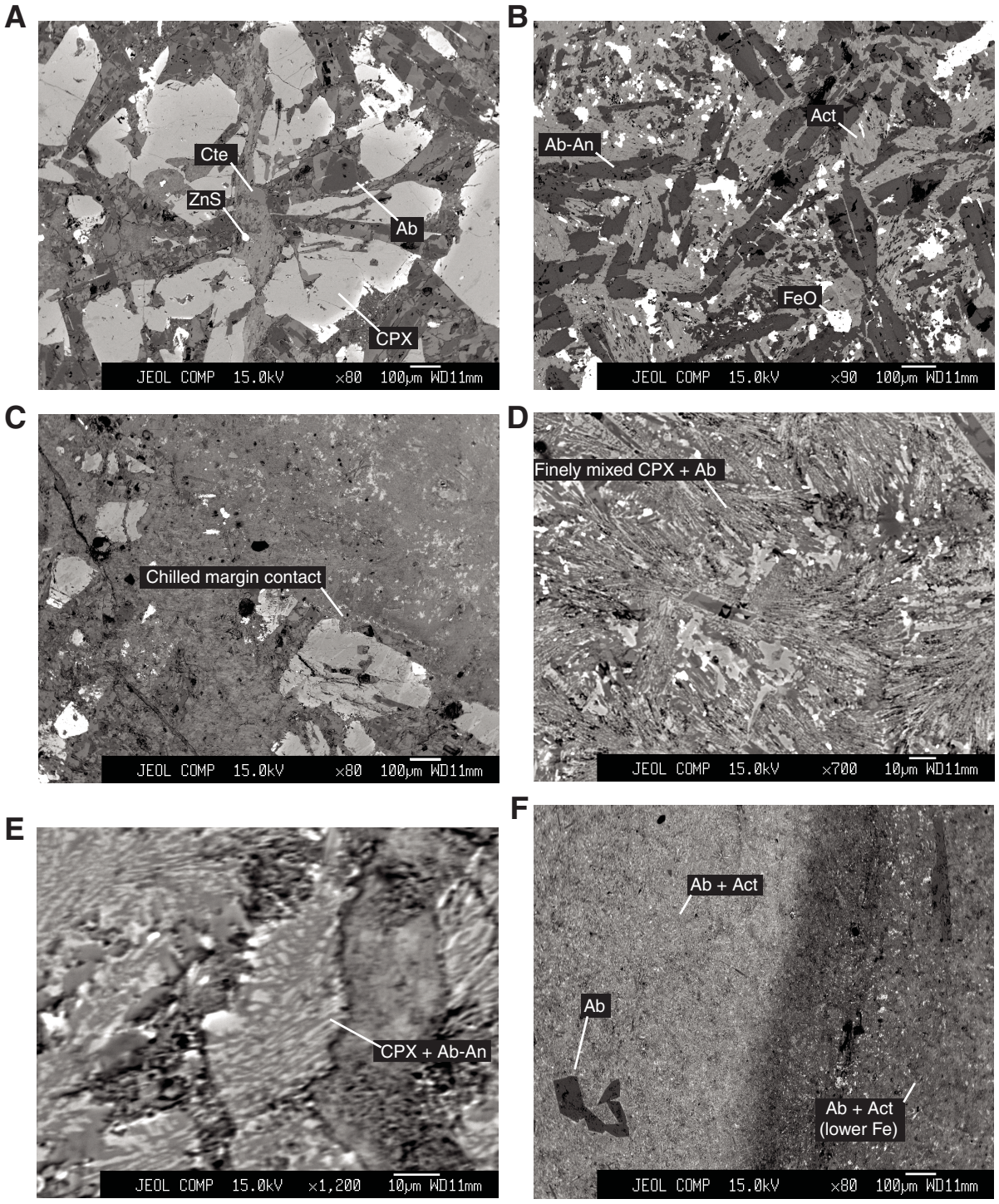

Figure F3. Chilled-margin microstructures. **A.** Albite (Ab) crysts with a weak preferred orientation surrounded by aggregates of aphanatic chlorite (Chl) (Sample 309-1256D-149R-1, 76–79 cm). **B.** Micrometer-scale grains of magnetite-ilmenite (Mag-Ilm) superposed on a chilled margin (Sample 312-1256D-187R-1, 75–77 cm). **C.** "Flow banding" defined by curving laminae of albite and chlorite (Sample 312-1256D-176R-2, 0–2 cm). At the lower part of the image are vugs of actinolite (Act). **D.** Flow microstructure defined by mixed actinolite and chlorite (Sample 312-1256D-187R-1, 75–77 cm). **E.** Spherulites composed of actinolite, albite-anorthite (Ab-An), and iron oxide, probably magnetite (FeO) (Sample 312-1256D-187R-1, 75–77 cm). F. A clast of anorthite (An) suspended in a chilled margin (Sample 312-1256D-187R-1, 75–77 cm).

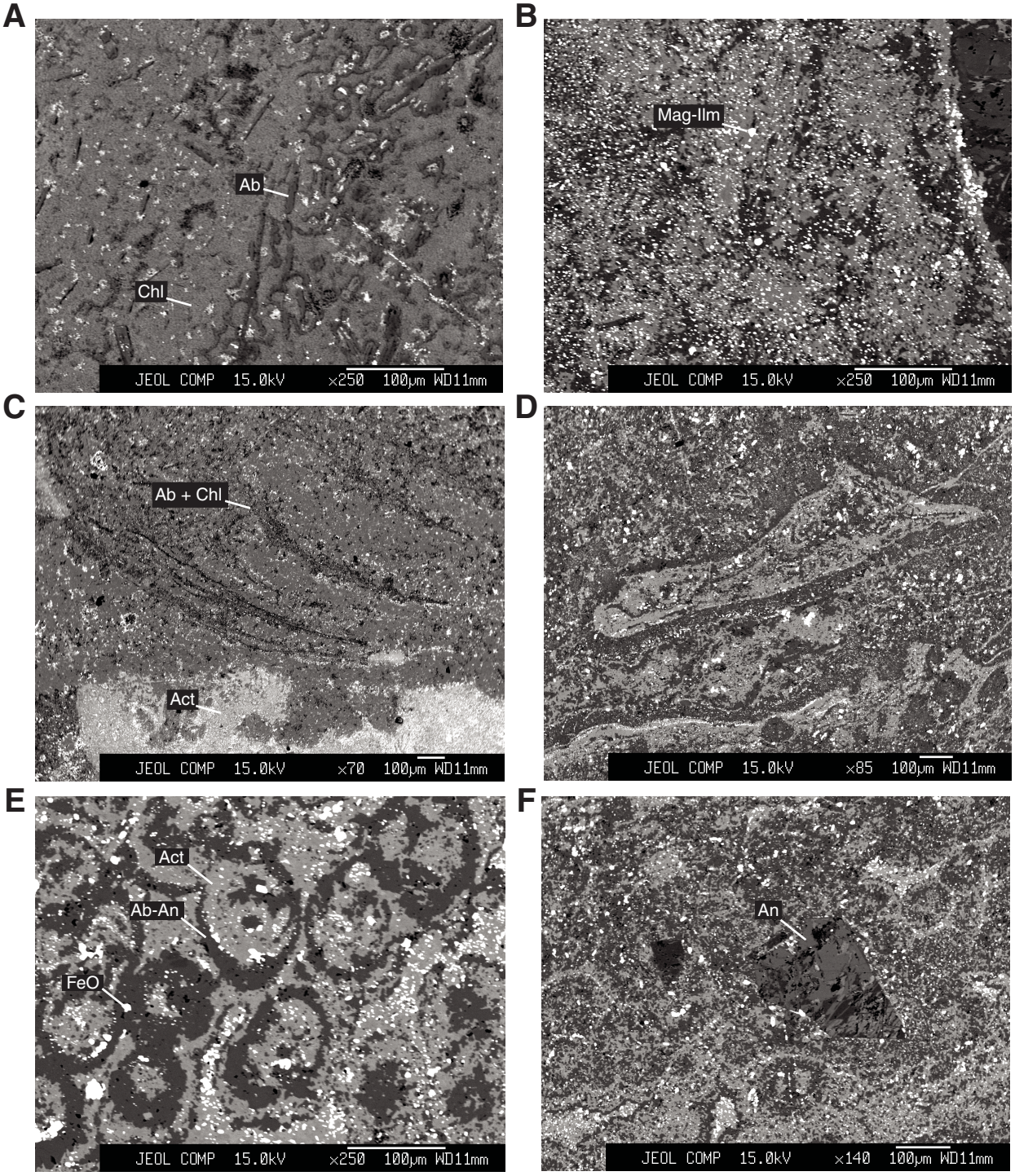

Figure F4. Chilled-margin veins. **A.** Elongate lens of sphene (titanite) and a crosscutting but parallel chlorite (Chl)-actinolite (Act) vein within a chilled margin (Sample 312-1256D-176R-2, 0–2 cm). **B.** Albite (Ab)-actinolite vein with irregular boundaries cutting across a chilled margin (Sample 312-1256D-187R-1, 75–77 cm). **C.** Anorthite (An) vein with chlorite vugs cuts across an actinolite vein (Sample 312-1256D-176R-2, 0-2 cm).

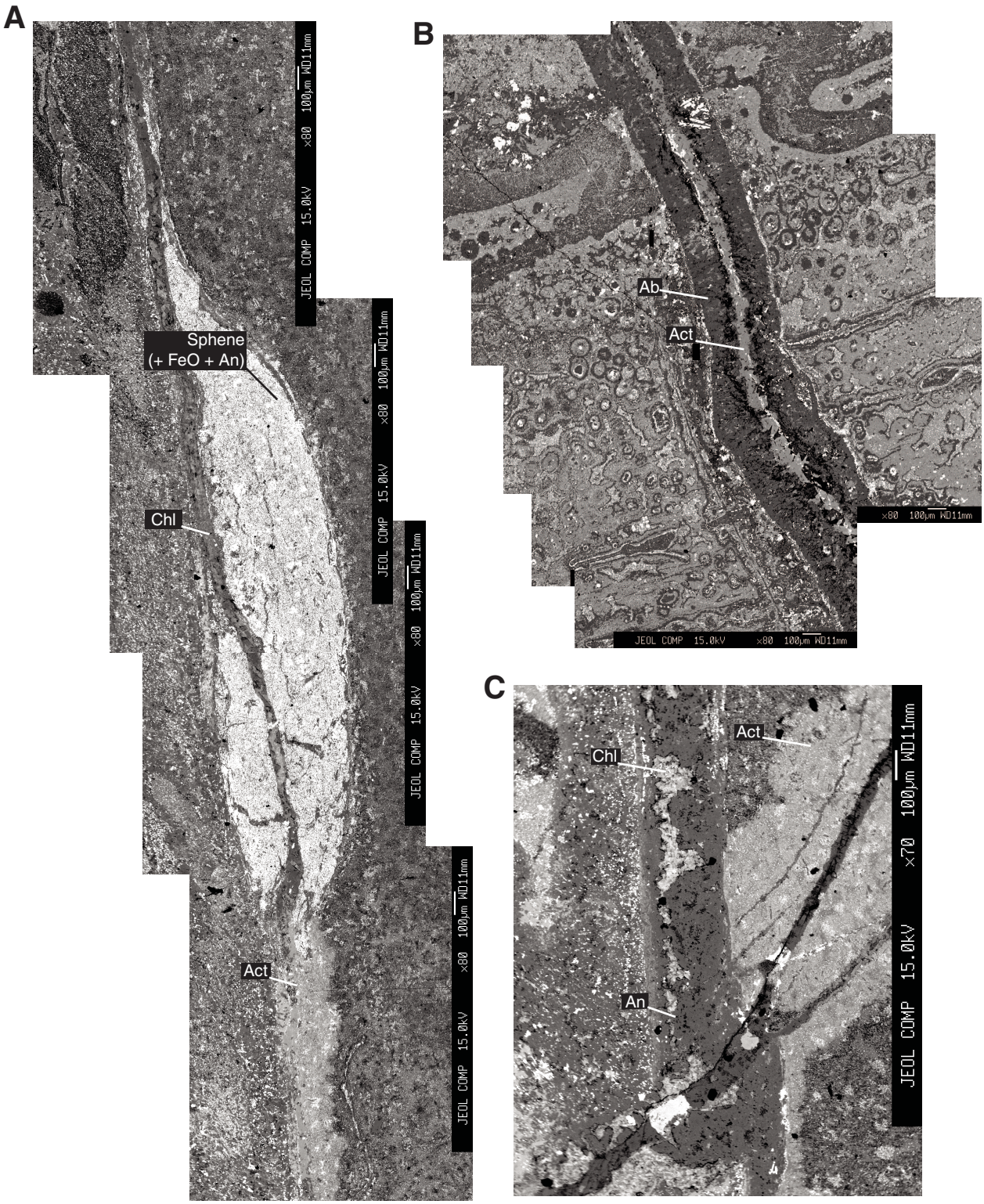

Figure F5. Chilled-margin alteration. **A.** Chlorite (Chl) vugs and veins (Sample 309-1256D-149R-1, 8–10 cm). **B.** Chlorite-quartz (Qtz) filled vug surrounded by chilled margin consisting of mixed anorthite-albite (An-Ab) and clinopyroxene (CPX) (Sample 309-1256D-143R-1, 34–38 cm). **C.** Clasts of quartz in a chilled margin (Sample 309-1256D-143R-1, 34–38 cm). Note fine, light gray banding in quartz grains is compositionally indistinguishable from the surrounding quartz in electron dispersive spectroscopy. **D.** Pyrite grains (FeS) mixed with anorthite and quartz (Sample 309-1256D-149R-1, 76–79 cm). **E.** Vein of anhydrite, actinolite (Act), and chlorite (Sample 309-1256D-161R-2, 6–8 cm). **F.** Anhydrite surrounded by blades of iron oxide (Sample 309-1256D-149R-1, 76–79 cm).

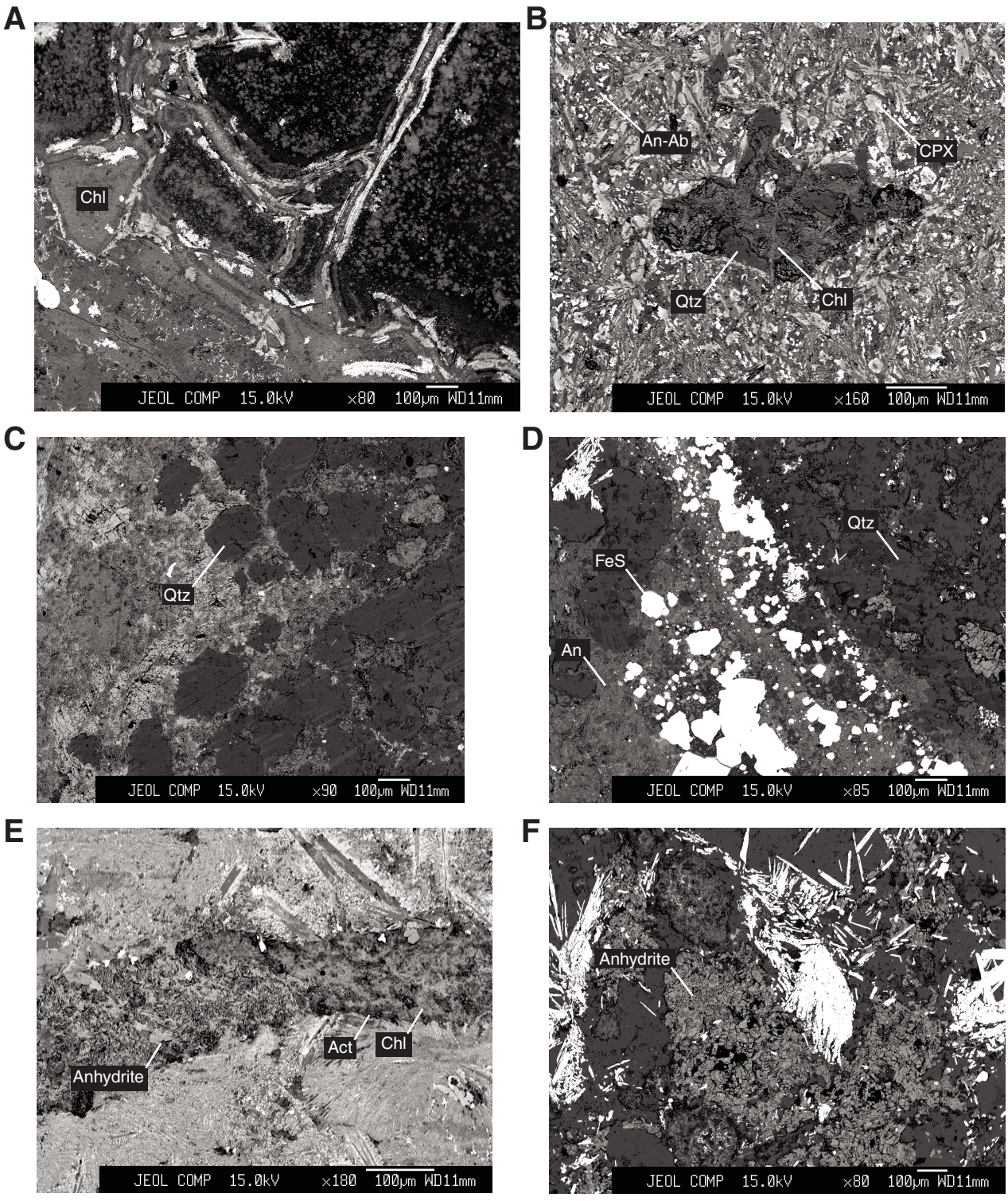

Figure F6. Orthoclase in chilled margins. **A.** Orthoclase (OR) in feldspar crystal cut by a chilled margin comprising aphanitic aggregate of chlorite (Chl) (Sample 309-1256D-136R-1, 4–6 cm). **B.** Interstitial orthoclase and chlorite in host rock adjacent to chilled margin (Sample 309-1256D-136R-1, 4–6 cm). **C.** Orthoclase and albite (Ab) in a feldspar phenocryst (Sample 309-1256D-161R-2, 6–8 cm). **D.** Vein of chlorite and chalcopyrite (CuFeS) and a small nodule of NaCl. The larger feldspar grain cut by the vein is rich in orthoclase (Sample 309-1256D-161R-2, 6–8 cm). **E.** Orthoclase-rich clast suspended in a chilled margin (Sample 309-1256D-136R-1, 4–6 cm). **F.** Mixed albite and anorthite (An) adjacent to a clinopyroxene cryst, adjacent to an orthoclase cryst, suspended in a chilled margin (Sample 309-1256D-161R-2, 6–8 cm).

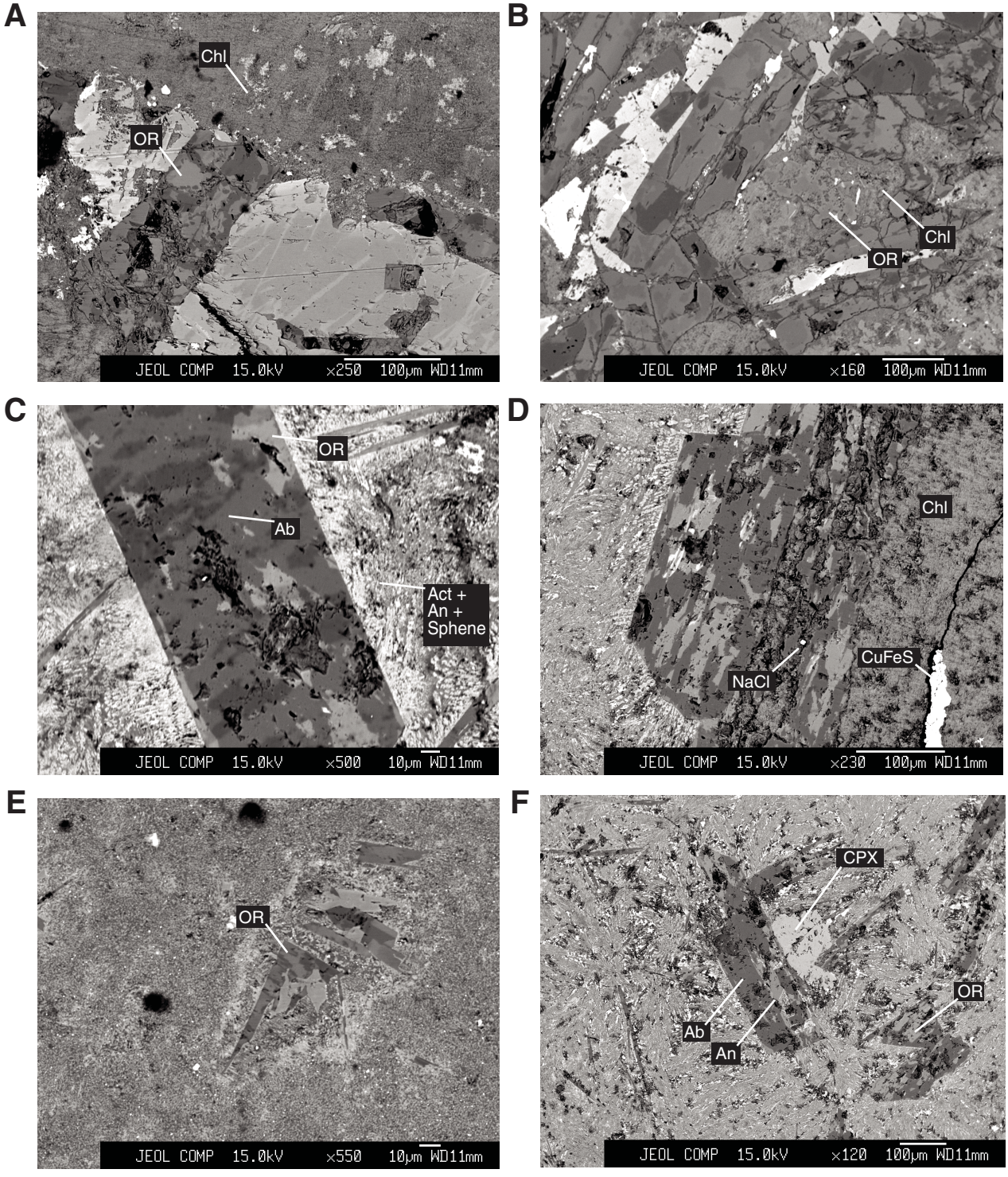

Figure F7. Feldspar wavelength dispersive spectroscopy compositions. **A.** Ternary diagram of feldspar analyses. An = anorthite, Ab = albite, Or = orthoclase. **B.** Plot of SrO vs. BaO for all analyses. **C.** Plot of K_2O vs. BaO for all analyses.

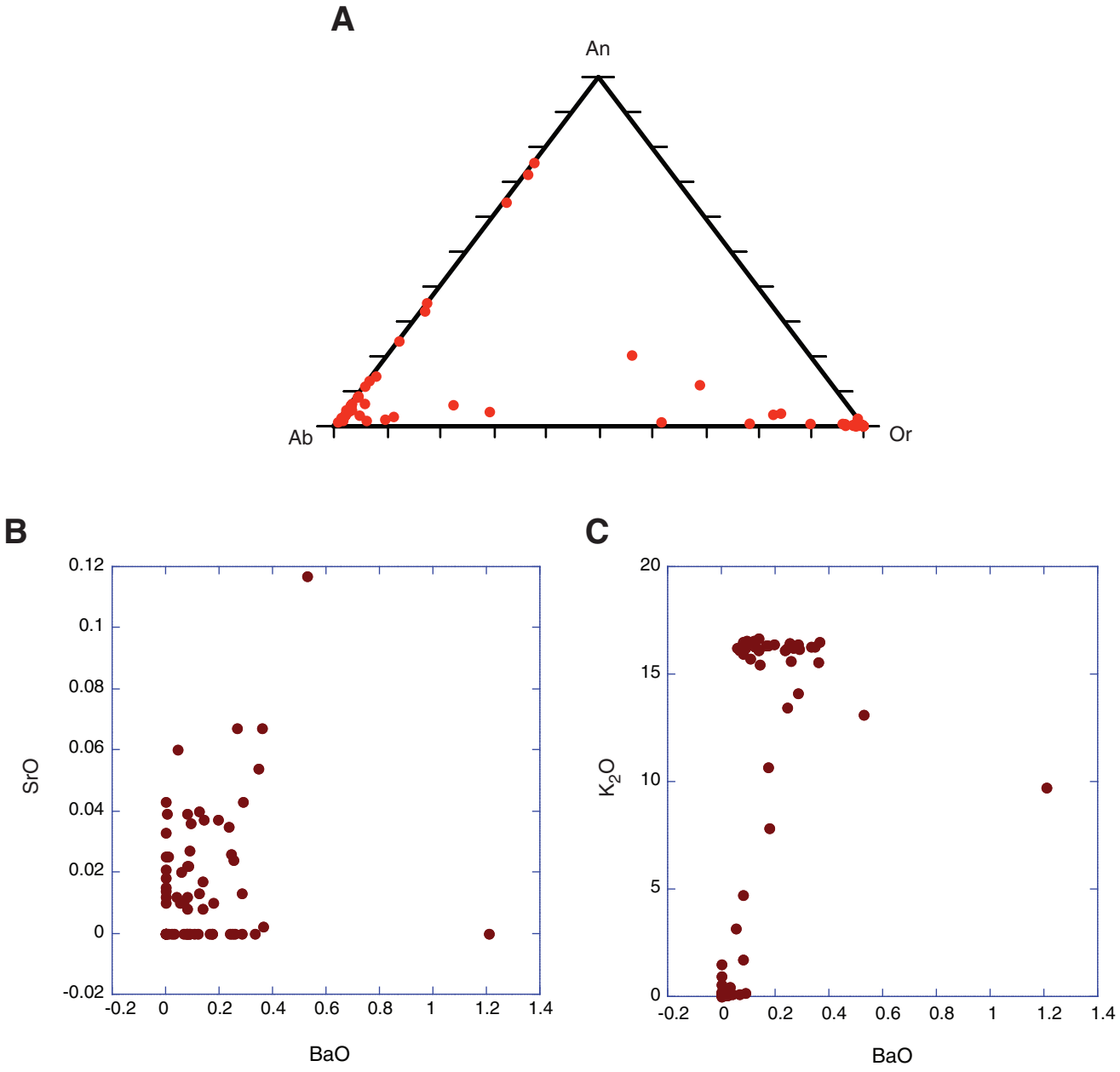

Table T1. Element oxide composition. (See table notes.) (Continued on next page.)

Core, section, interval (cm)	Structure	Major element oxides (wt%)							
		SiO_2	Al_2O_3	CaO	Na_2O	K_2O	BaO	SrO	Total
309-1256D-									
136R-1, 4–6	1-adjacent to CM	64.137	19.82	6.012	10.314	0.067	0.023	0	100.373
136R-1, 4–6	1-adjacent to CM	57.221	17.795	20.331	4.252	0.175	0	0	99.774
136R-1, 4–6	1-adjacent to CM	64.419	18.155	0.677	1.755	14.112	0.286	0.013	99.417
136R-1, 4–6	1-adjacent to CM	65.275	18.262	0.066	0.196	16.188	0.289	0.043	100.319
136R-1, 4–6	1-adjacent to CM	68.778	19.69	0.553	9.978	1.752	0.081	0.039	100.871
136R-1, 4–6	1-adjacent to CM	65.717	18.217	0.038	0.118	16.228	0.267	0.067	100.652
136R-1, 4–6	1-adjacent to CM	59.583	24.326	6.721	7.482	0.151	0.088	0.027	98.378
136R-1, 4–6	1-adjacent to CM	62.092	21.677	4.094	3.741	7.841	0.178	0.01	99.633
136R-1, 4–6	1-adjacent to CM	64.788	17.988	0.129	0.384	15.566	0.358	0.067	99.28
136R-1, 4–6	1-adjacent to CM	65.424	21.13	2.549	9.581	—	0.045	0.06	98.789
136R-1, 4–6	2-adjacent to CM	64.605	18.554	0.701	1.472	13.44	0.245	0.026	99.043
136R-1, 4–6	2 adjacent to CM	65.152	17.792	0.077	0.15	16.111	0.236	0.035	99.553
136R-1, 4–6	2-adjacent to CM	59.506	24.828	7.01	7.117	0.016	0.002	0.014	98.493
136R-1, 4–6	2-adjacent to CM	64.927	21.457	2.829	9.306	0.164	0	0	98.683
136R-1, 4–6	2-adjacent to CM	54.179	28.575	12.161	3.704	0.107	0.068	0	98.794
136R-1, 4–6	3-adjacent to CM	67.023	20.18	1.246	9.781	0.454	0.032	0	98.716
136R-1, 4–6	3-adjacent to CM	68.383	20.251	1.169	10.32	0.062	0.009	0.025	100.219
136R-1, 4–6	3-adjacent to CM	64.601	18.271	0.064	0.154	16.143	0.24	0	99.473
136R-1, 4–6	3-adjacent to CM	63.018	20.342	2.36	2.771	10.668	0.172	0	99.331
136R-1, 4–6	3-adjacent to CM	64.797	18.722	0.146	2.331	13.126	0.53	0.117	99.769
136R-1, 4–6	3-adjacent to CM	65.151	18.257	0.114	0.339	15.602	0.257	0	99.72
136R-1, 4–6	3-adjacent to CM	64.884	18.215	0.058	0.13	16.268	0.248	0	99.803
136R-1, 4–6	4-adjacent to CM	64.87	18.148	0.014	—	16.107	0.136	0.017	99.292
136R-1, 4–6	4-adjacent to CM	65.191	18.173	0.004	—	16.207	0.09	0	99.665
136R-1, 4–6	4-adjacent to CM	65.271	18.164	0.009	—	16.212	0.076	0	99.732
136R-1, 4–6	4-adjacent to CM	64.927	18.105	0.013	—	16.242	0.057	0.02	99.364
136R-1, 4–6	4-adjacent to CM	49.834	30.944	14.885	2.661	0.04	0	0	98.364
136R-1, 4–6	4-adjacent to CM	68.525	19.555	0.222	10.875	0.061	0	0	99.238
136R-1, 4–6	4-adjacent to CM	69.363	20.031	0.823	10.121	0.152	0	0	100.49
136R-1, 4–6	4-adjacent to CM	65.685	18.618	0.027	—	16.488	0.363	0.002	101.183
136R-1, 4–6	4-adjacent to CM	65.565	18.15	0.049	—	16.44	0.253	0.024	100.481
136R-1, 4–6	4-adjacent to CM	65.718	19.891	0.211	3.907	9.705	1.209	0	100.641
136R-1, 4–6	4-adjacent to CM	65.321	18.232	0.054	—	16.395	0.283	0	100.285
136R-1, 4–6	4-adjacent to CM	67.341	21.137	1.725	10.15	0.084	0	0.018	100.455
136R-1, 4–6	4-adjacent to CM	68.585	20.999	1.293	10.434	0.061	0	0.033	101.405
161R-2, 6–8	5-within CM	65.759	17.864	0.419	—	15.953	0.078	0	100.073
161R-2, 6–8	5-within CM	70.009	19.869	0.314	10.584	0.96	0	0	101.736
161R-2, 6–8	5-within CM	68.749	20.705	1.693	10.355	0.088	0	0	101.59
161R-2, 6–8	5-within CM	65.465	18.229	0.025	0.355	15.752	0.109	0	99.935
161R-2, 6–8	5-within CM	64.554	18.063	0.028	—	16.285	0.332	0	99.262
161R-2, 6–8	5-within CM	68.213	19.754	0.731	10.635	0.124	0	0	99.457
161R-2, 6–8	5-within CM	68.632	19.82	0.579	10.713	0.129	0	0	99.873
161R-2, 6–8	5-within CM	65.459	21.269	1.159	7.904	3.179	0.055	0.01	99.035
161R-2, 6–8	6-within CM	64.182	17.829	0.04	—	16.131	0.067	0.01	98.259
161R-2, 6–8	6-within CM	65.943	18.282	0.037	—	16.453	0.078	0.008	100.801
161R-2, 6–8	6-within CM	65.862	18.371	0.136	1.095	15.434	0.143	0.037	101.078
161R-2, 6–8	6-within CM	65.12	18.324	0.027	0.197	16.275	0.345	0.054	100.342
161R-2, 6–8	6-within CM	68.351	20.027	0.959	11.06	0.033	0	0.01	100.44
161R-2, 6–8	6-within CM	66.717	19.375	0.834	7.732	4.719	0.079	0.012	99.468
161R-2, 6–8	6-within CM	68.207	19.727	0.691	11.265	0.128	0.039	0.012	100.069
161R-2, 6–8	6-within CM	66.533	19.594	1.098	10.766	—	0	0.015	98.006
161R-2, 6–8	6-within CM	66.864	19.889	1.22	10.416	0.072	0	0.025	98.486
161R-2, 6–8	6-within CM	68.372	19.442	0.482	11.011	0.067	0	0	99.374
161R-2, 6–8	6-within CM	68.444	19.628	0.922	10.453	0.209	0.001	0.012	99.669
161R-2, 6–8	7-adjacent to CM	65.691	18.432	0.012	—	16.509	0.089	0	100.733
161R-2, 6–8	7-adjacent to CM	65.608	18.33	0.003	—	16.548	0.122	0	100.611
161R-2, 6–8	7-adjacent to CM	65.046	18.437	—	—	16.402	0.197	0.037	100.119
161R-2, 6–8	7-adjacent to CM	65.566	18.2	—	—	16.49	0.081	0	100.337
161R-2, 6–8	7-adjacent to CM	64.546	18.006	0.002	—	16.253	0.126	0.04	98.973
161R-2, 6–8	7-adjacent to CM	64.175	17.923	0.024	—	16.312	0.174	0	98.608
161R-2, 6–8	7-adjacent to CM	65.621	21.034	2.304	9.915	0.062	0.005	0.039	98.98
161R-2, 6–8	7-adjacent to CM	66.51	22.237	2.706	10.039	0.067	0.007	0	101.566
161R-2, 6–8	7-adjacent to CM	65.494	17.978	0.031	0.155	16.27	0.125	0.013	100.066
161R-2, 6–8	8-vein near CM	65.258	17.87	0.031	0.128	16.406	0.08	0.022	99.795
161R-2, 6–8	8-vein near CM	65.261	18.078	0.027	0.171	16.314	0.164	0	100.015
161R-2, 6–8	8-vein near CM	65.249	18.104	0.024	0.152	16.468	0.086	0.022	100.105
161R-2, 6–8	8-vein near CM	65.091	17.952	0.026	0.1	16.541	0.095	0.036	99.841

Table T1 (continued).

Core, section, interval (cm)	Structure	Major element oxides (wt%)							
		SiO_2	Al_2O_3	CaO	Na_2O	K_2O	BaO	SrO	Total
161R-2, 6–8	8-vein near CM	65.418	17.928	0.02	0.145	16.661	0.137	0.008	100.317
161R-2, 6–8	8-vein near CM	66.96	20.245	0.599	10.189	0.576	0	0	98.569
161R-2, 6–8	8-vein near CM	62.234	23.644	5.694	8.303	—	0	0.043	99.918
161R-2, 6–8	8-vein near CM	68.767	19.691	0.703	10.976	—	0	0	100.137
161R-2, 6–8	8-vein near CM	68.956	19.694	0.648	10.891	0.123	0	0	100.312
161R-2, 6–8	8-vein near CM	68.293	19.593	0.539	10.874	0.126	0	0	99.425
161R-2, 6–8	8-vein near CM	68.058	19.084	0.374	9.834	1.486	0	0.021	98.857
161R-2, 6–8	8-vein near CM	68.547	19.385	0.311	10.871	0.189	0	0	99.303

Notes: CM = chilled margin. — = no data.